Title: Design Optimization of a Solenoid-based Electromagnetic Soft Actuator with Permanent Magnet Core

Nafiseh Ebrahimi*,

*Corresponding author: Mechanical Engineering Department, University of Texas at San Antonio (UTSA), One UTSA Circle San Antonio, 78249, TX, USA. nafiseh.ebrahimi@utsa.edu

Paul Schimpf[a],

[a] Department of Computer Science, Eastern Washington University (EWU), Cheney, 99004, WA, USA. pschimpf@ewu.edu

Amir Jafari[b], [b] Mechanical Engineering Department, the University of Texas at San Antonio (UTSA), One UTSA Circle San Antonio, 78249, TX, USA. amir.jafari@utsa.edu

Abstract

This paper discusses design optimization of an electromagnetic soft actuator composes of two antagonistic solenoids that share a permanent magnet core. First, calculation of the magnetic field and applied force of a solenoid with a permanent magnet plunger is presented as the principal component of this electromagnetic actuator. Design optimization of the coil is discussed considering the geometrical parameters of the coil, including its length, inner and average diameters, number of turns and packing density while the power consumption is bounded. The impact of the actuator size on the resultant force is presented and scaling limitations are discussed. Then, due to the soft nature of the actuator's component, the impact of the cross-section, i.e. lateral deformation of the actuator on the magnetic field at the center of section investigated as well. The deformation might happen to the actuator due to the load in the transverse direction, especially when the actuator is made of flexible materials.

Keywords

Electromagnetic actuator, optimization, Biot-Savart law, solenoid, magnetic core

1. Introduction

Electromagnetic actuators are gaining interests among researchers due to many advantages including short response time, simple controllability, an uncomplicated structure in comparison to the other types of the actuator (Song and Lee 2015; Petit et al. 2010).

The design, optimization, and application of the solenoid as a vastly used electromagnetic actuator has been considered by many researchers in recent years. A solenoid is composed of a coil that is an electrically conductive wire warped around a magnetically permeable cylindrical core, i.e. plunger. When an electric current passes through the coil, it generates a magnetic field that can act upon the plunger and create electromagnetic force. These type of linear actuators have been serving numerous applications ranging from measurement systems to manufacturing. (Banick and Haller 1991) designed a solenoid actuator equipped with a magnetic flux sensor capable to indicate the position of the solenoid core. (Lim, Cheung, and Rahman 1994) proposed a method for proportional control of a solenoid actuator to convert its switching mode into a proportional actuator. (Mitsutake, Hirata, and Ishihara 1997) applied finite element method to predict the dynamic response characteristics of a linear solenoid actuator. (Kamal and Daehn 2007) presented an analysis for the coil to design an electromagnetic actuator for flat sheet forming purposes. (Petit et al. 2010) proposed a four-discrete-position electromagnetic actuator, then presented its modeling and also experiments. (Shin et al. 2011) developed a biomimetic actuator using four segmented solenoids mimicking earthworm movements. (Fries et al. 2014) fabricated an electromagnetically driven elastic actuator proper for use as muscle-like structures, capable to generate stress and strain when embedded in a solenoid coil. (Song and Lee 2015) developed a solenoid actuator having a ferromagnetic plunger and applied the solenoid actuator in a multi-segmented miniaturized robot to generate both rectilinear and turning movements. (Said et al. 2016) designed and fabricated a compact electromagnetically driven micro actuator using Polydimethylsiloxane (PDMS) and embedded magnetic particles. (Rawlik et al. 2017) presented a method to design a coil generating an arbitrarily shaped magnetic field. (Guo et al. 2018) demonstrated the fabrication of a soft electromagnetic actuator using liquid metal coil of Ga-In alloy for soft robotic applications. Nevertheless, there is still a deficiency in coil design optimization in order to generate the optimum possible field and force out of the solenoid actuator.

Previously, we discussed the design, development, and control of an electromagnetic soft actuator for rehabilitation application that comprises of two solenoid coils and a common magnetic core. This actuator is entirely made of soft materials and is highly scalable (Ebrahimi et al. 2018). The actuator body is made of Silicone polymer PDMS with embedded helical micro-channels. Eutectic GalliumIndium EGaIn that is a conductive liquid in room temperature was injected into micro-channels creating conductive coils. Magnetic particles mixed with PDMS and placed into a strong magnetic field during the curing process to force magnetic particles to stay aligned together once the external magnetic field was removed. The result is a soft permeant magnet which was placed into the solenoids as the core. In this paper, we propose an electromagnetic actuator presented in Figure 1, consists of two coils and a permanent magnet plunger in the middle interacting with the coils to generate linear motion and force. The magnetic plunger was applied in order to generate higher actuation forces compared to the ferromagnetic core (Song and Lee 2015). Moreover, this magnetic plunger is shared between two coils to benefit the entire volume of the magnet to raise the generated force compared to the generic solenoid actuators.

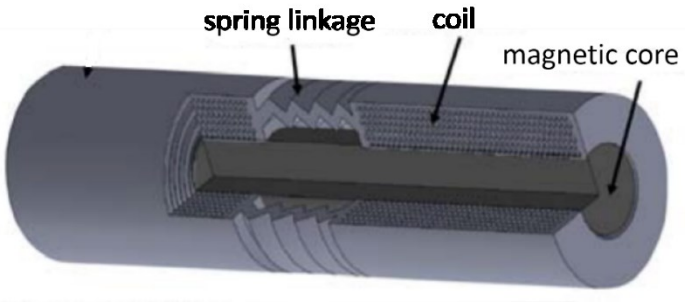

Figure 1. Schematic of electromagnetic actuator

We intended to find a proper configuration for the components as well as solenoid design characteristics in order to exert maximum output force out of the actuator. To achieve this goal, we implemented our theoretical analysis using the Biot-Savart law (Panofsky and Phillips 2012) to calculate the magnetic field of the solenoid on the axis. Then, the applied force of the solenoid upon the permanent magnet plunger and the total applied force of the electromagnetic actuator were derived utilizing Charge model (Furlani 2001; Pratt 2008). Then, the geometrical design of the solenoid and plunger was considered in next steps applying the analytical results for the magnetic field and force. The influence of cylindrical cross-section deformation on the magnetic field at the center of the solenoid was investigated as well.

2. *Solenoid Magnetic Field and Force Calculation*

Our proposed actuator is composed of two electromagnetically inductive solenoids combined with permanent magnet plungers. The force generated by the solenoid depends on several factors including a number of turns, coil's length and diameter, applied current, permanent magnet's length, diameter, and material.

To design the electromagnetic actuator, a theoretical analysis was conducted on the electromagnetic force produced by two solenoids encompass a common permanent magnetic core. For this purpose, firstly the Biot-Savat law calculates the magnetic field along the axis of a loop passing steady current at the arbitrary point P. Applying Bio-Savart law, the contribution of the current element (Figure 2) to the magnetic field at point *P* is expressed by equation 1 (Grandy 2012; Panofsky and Phillips 2012):

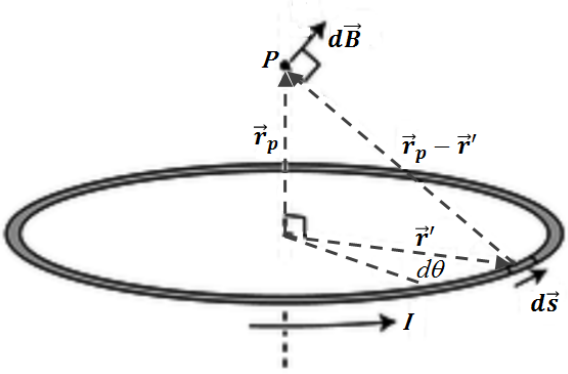

Figure 2. Magnetic field at the desired point caused by a single circular current element; $d\vec{B}$: differential element of magnetic field at the center of the current element, $\vec{r}_p$: axial position vector of the arbitrary point P, $\vec{r}'$: radial position vector of the arbitrary point P (radius vector), I: flowing current, $d\vec{s}$: differential length element on the circular current carrying loop.

$$d\vec{\mathbf{B}} = \frac{\mu_0}{4\pi}\frac{d\vec{\mathbf{s}}\times\mathbf{r}}{r^2} = \frac{\mu_0 I}{4\pi}\frac{d\vec{s}\times\vec{r}}{r^3} = \frac{\mu_0 I}{4\pi}\frac{d\vec{s}\times(\vec{r}_p-\vec{r})}{|\vec{r}_p-\vec{r}|} \qquad (1)$$

Where $d\vec{\mathbf{s}} = Rd\theta\hat{\boldsymbol{\theta}}$, $\vec{\mathbf{r}}_p = z\hat{\mathbf{k}}$, and $\vec{\mathbf{r}} = R\hat{\mathbf{r}}$, and *R* is the magnitude of the radius vector ($\vec{\mathbf{r}}$) or coil radius shown in Figure 3. Also, z is the coordinate along the solenoid axis and $\hat{\mathbf{k}}$ is the unit vector in z direction.

$$d\vec{\mathbf{B}} = \frac{\mu_0}{4\pi}\frac{Rd\theta\hat{\boldsymbol{\theta}})\times(z\hat{\mathbf{k}}-R\hat{\mathbf{r}})}{|z\hat{\mathbf{k}}-R\hat{\mathbf{r}}|^3} \qquad (2)$$

$$= \frac{\mu_0 IzR}{4\pi(z^2+R^2)^{3/2}} d\theta\hat{\mathbf{r}} + \frac{\mu_0 IR^2}{4\pi(z^2+R^2)^{3/2}} d\theta\hat{\mathbf{k}}$$

Integrating over the entire circular loop results the magnetic field at *P*. The first integral vanishes due to the equal magnitude and the fact that radial unit vectors around the circle sum to zero. Hence, the remaining is just the axial component of the magnetic field (equation 3).

$$\vec{\mathbf{B}}_Z = \frac{\mu_0 IR^2}{4\pi(z^2+R^2)^{3/2}} \int_0^{2\pi} d\theta\hat{\mathbf{k}} = \frac{\mu_0 IR^2}{2(z^2+R^2)^{3/2}} \hat{\mathbf{k}} \qquad (3)$$

For a finite solenoid consisting of a large number of circular loops using the result obtained above for the magnetic field of one loop, the magnetic field at point *P* on the axis of solenoid could be obtained by integrating over the entire length. Figure 3 shows the selected current element on the solenoid. The *z* dimension of the selected point (*P*) is always measured from the central loop of the solenoid. The amount of current passing through the element is given by

$dI = I\ (ndz') = I\ (N/l)\ dz'$, where $n = N/l$ is the number of turns per unit length or turn density.

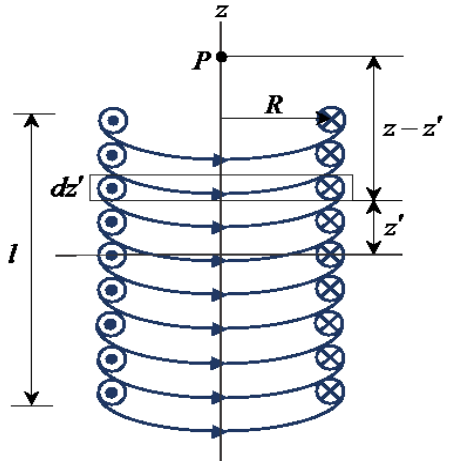

Figure 3. Magnetic field at a desired point generated by a schematic coil; l: solenoid length, R: solenoid radius, z: axial distance of the desired point P to the center of the solenoid and along its axis, dz' : differential current element thickness, z' : axial distance of current element to the center of the solenoid.

Applying equation 3, the contribution to the magnetic field at *P* caused by the current element with a thickness of dz' is:

$$dB_z = \frac{\mu_0 R^2}{2[(z-z')^2+R^2]^{3/2}} dI = \frac{\mu_0 R^2}{2[(z-z')^2+R^2]^{3/2}} (nIdz') \qquad (4)$$

Integrating over the solenoid length, we obtain:

$$B_z = \frac{\mu_0 nIR^2}{2} \int_{-l/2}^{l/2} \frac{dz'}{[(z-z')^2+R^2]^{3/2}}$$

$$= \frac{\mu_0 nIR^2}{2} \frac{z'-z}{R^2\sqrt{(z-z')^2+R^2}} \Big|_{-l/2}^{l/2} \qquad (5)$$

$$= \frac{\mu_0 nI}{2} \left[\frac{(l/2)-z}{\sqrt{(z-l/2)^2+R^2}} + \frac{(l/2)+z}{\sqrt{(z+l/2)^2+R^2}} \right]$$

Equation 5 expresses the magnetic field of a finite solenoid at the desired point P with a distance of z from the center of the solenoid. For our electromagnetic actuator system, we need to take into account the contribution of both coils on the particular point we are interested to find the magnetic field. Using the result obtained above for a single solenoid and applying the superposition principle the magnetic field at the desired point on the common axis of two solenoids (*P*) is obtainable.

$$\mathbf{B}_z = \mathbf{B}_{right} + \mathbf{B}_{left} \qquad (6)$$

To calculate $\mathbf{B}_{right}$ and $\mathbf{B}_{left}$ in the equation 6, the distances of an arbitrary point P from the center of each coil $(z_1 \& z_2)$ should be determined as depicted in Figure 4.

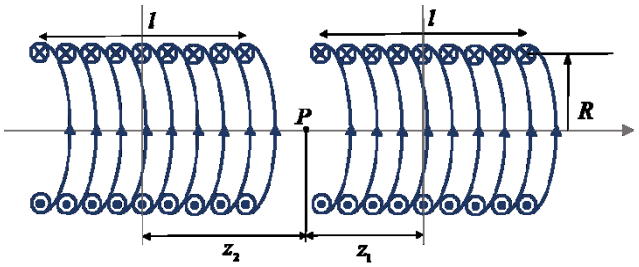

Figure 4. Magnetic field calculation at point P on the common axis of two schematic coaxial solenoids of the actuator; l: solenoid length, R: solenoid radius, z_1: axial distance of the arbitrary point P to the center of the right-hand solenoid, z_2 : axial distance of the arbitrary point P to the center of the left-hand solenoid.

Next step is the calculation of applied force to the magnetic core. Charge model is a useful method for analyzing permanent magnet such as determining the force and torque on a magnet located inside an external field. Based on charge model force can be expressed by equation 7 (Furlani 2001):

$$\mathrm{F} = \int \rho_m \mathbf{B}_{\mathbf{ext}} dv + \oint \sigma_m \mathbf{B}_{\mathbf{ext}} ds \qquad (7)$$

Where

$\rho_m = -\nabla \cdot \mathbf{M} (Amps/m^2)$ is equivalent volume charge density

$\sigma_m = \mathbf{M} \cdot \hat{n} (Amps/m)$ is equivalent surface charge density

In this case, $\mathbf{B}_{ext}$ is the superposed field calculated from equation 5 and 6 at any arbitrary point ($\mathbf{B}_p$). The magnetic core has a fixed and uniform magnetization along its axis expressed as follows:

$\mathbf{M} = M\hat{\mathbf{Z}}$

Therefore, $\rho_m = -\nabla \cdot \mathbf{M} = 0$

The magnetization, $\mathbf{M}$, is the net magnetic moment per unit volume of the permanent magnet and can be calculated using equation 8:

$$M = B_r / \mu_0 \qquad (8)$$

Where μ_0 is the vacuum permeability and B_r is a material property named remanence or residual flux density. It is an important factor for permanent magnets and is obtainable from the hysteresis curve of the material (Jiles 1998).

To calculate surface charge (σ_m) we first should determine the unit surface normal vectors on the magnet. The cylindrical magnet has three distinct surfaces as follows (Figure 5).

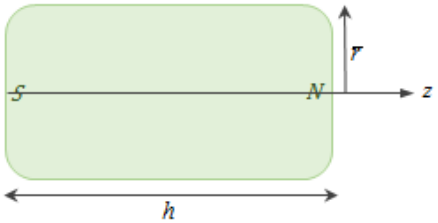

Figure 5. Magnet core dimensions; $\bar{r}$: permanent magnet radius, h: permanent magnet length

$$\hat{n} = \begin{cases} -\hat{\mathbf{z}} & z = 0 \\ \hat{\mathbf{z}} & z = h \\ \hat{\mathbf{r}} & r = \bar{r} \end{cases}$$

Where h and r are the magnet core length and radius respectively. Also, $\hat{z}$ and $\hat{r}$ are unit vectors in axial and radial directions.

Then, the surface charge density $\sigma_m = \mathbf{M} \cdot \hat{n}$ obtained as:

$$\sigma_m = \begin{cases} -M_s & z = 0 \\ M_s & z = h \end{cases} \qquad (9)$$

Where M_s is the magnetization of the magnetic core along the z axis. It is notable that for the cylindrical surface of the magnet, $\sigma_m = \mathbf{M} \cdot \hat{n} = 0$ since the two vectors are perpendicular to each other. The North Pole surface of the magnetic core is located in the right solenoid and the South Pole surface is located in the left one (Figure 6). Dimension d in this figure expresses the distance between the magnet pole and the related coil middle point.

The magnetic core located exactly at the middle of the line connecting the two coils, so, each pole has the same distance to the correlated coil's end (d) . Due to the symmetric geometry of the actuator, we just need to calculate the force applied to one end surface of the magnetic core and then double it to obtain the total applied force. These two forces are identical in magnitude but have opposite directions. If we consider the North Pole of the magnet, firstly we need to calculate $\mathbf{B}_{\text{ext}}$ at this point. Choosing an arbitrary point, P, on the North Pole z_1 and z_2 could be calculated as: $z_1 = d$ and $z_2 = d + h$.

Applying equations 5 and 7 the contributions of both coils at this specific point could be calculated and superposed.

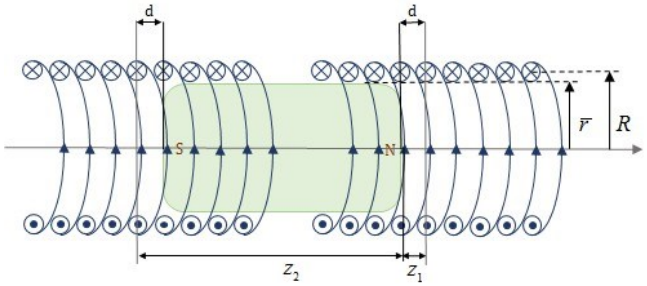

Figure 6. The configuration of the electromagnetic actuator with two schematic coils and common magnetic core; R: solenoid radius, $\bar{r}$: permanent magnet radius, d: axial distance from each magnet pole to the center of related solenoid, z_1 : distance between North pole and the center of the right solenoid, z_2 : distance between North Pole and the center of the left solenoid.

$$\mathbf{B}_{right} = \frac{\mu_0 nI}{2}\left[\frac{(l/2)+d}{\sqrt{(-d-(l/2))^2+R^2}} + \frac{(l/2)-d}{\sqrt{(-d+(l/2))^2+R^2}}\right]$$
$$\mathbf{B}_{left} = \frac{\mu_0 nI}{2}\left[\frac{(l/2)-(d+h)}{\sqrt{(d+h-(l/2))^2+R^2}} + \frac{(l/2)+(d+h)}{\sqrt{(d+h+(l/2))^2+R^2}}\right] \qquad (10)$$

Having the same current directions in two coils results in same direction magnetic field vectors algebraically added together (equation 11).

$$B_{ext} = B_{right} + B_{left}$$
$$= \frac{\mu_0 nI}{2}\left[\begin{array}{l} \dfrac{(l/2)+d}{\sqrt{(-d-(l/2))^2+R^2}} + \dfrac{(l/2)-d}{\sqrt{(-d+(l/2))^2+R^2}} \\ + \dfrac{(l/2)-(d+h)}{\sqrt{(d+h-(l/2))^2+R^2}} + \dfrac{(l/2)+(d+h)}{\sqrt{(d+h+(l/2))^2+R^2}} \end{array}\right] \qquad (11)$$

Hence, applying equation 8, the force on the magnetic core is obtained:

$$\mathrm{F} = \oint \sigma_m \mathbf{B_{ext}} ds = \mathbf{B_{ext}} M \int_0^{\vec{r}} \int_0^{2\pi} r dr d\emptyset = \mathbf{B_{ext}} \frac{B_r}{\mu_0} \pi \bar{r}^2 \qquad (12)$$

Substituting equation 12 into 13 results force applied to the North Pole of the magnetic core, generated by two right and left coils' magnetic fields (equation 12

$$F = \frac{nIB_r}{2} \pi \bar{r}^2 \left[\frac{(l/2)+d}{\sqrt{(d+(l/2))^2+R^2}} + \frac{(l/2)-d}{\sqrt{(-d+(l/2))^2+R^2}} + \frac{(l/2)-(d+h)}{\sqrt{(d+h-(l/2))^2+R^2}} + \frac{(l/2)+(d+h)}{\sqrt{(d+h+(l/2))^2+R^2}} \right] \qquad (13)$$

The same story goes true for the South Pole. Regarding the symmetry, the South Pole experiences the same amount of force on the correlated surface. Hence, equation 15 expresses the whole amount of force applied to the magnet core :

$$F_{total} = 2F$$
$$= nIB_r \pi \bar{r}^2 \left[\frac{(l/2)+d}{\sqrt{(d+(l/2))^2+R^2}} + \frac{(l/2)-d}{\sqrt{(-d+(l/2))^2+R^2}} + \frac{(l/2)-(d+h)}{\sqrt{(d+h-(l/2))^2+R^2}} + \frac{(l/2)+(d+h)}{\sqrt{(d+h+(l/2))^2+R^2}} \right] \qquad (14)$$

The maximum magnetic field and consequently, solenoid force occurs at the center of the coil. Hence, the centers of the coils would be the best place for positioning the permanent magnet base surfaces or poles ($d = 0$ in equations 11 and 13). Exerting the two equations, Figure 7(a) and 7(b) depict such an actuator net magnetic field and force variations respectively in terms of inner diameter (d_i). In this analysis, some of the parameters get fixed as follows: the coil wire length ($l_w = 3m$), the applied current to the actuator coils ($i = 0.33amp$) based on ("American Wire Gauge Chart and AWG Electrical Current Load Limits Table with Skin Depth Frequencies and Wire Breaking Strength" n.d.), the permanent magnet length ($h = 10mm$), the radial air-gap between magnet core and coils coils ($g = 0.2mm$), magnet core residual flux density ($B_r = 0.18T$) and the wire gauge ($34AWG$). We tried to find the optimum amount of inner diameter for a one-layer coil made by a fixed wire length ($l_w = 3m$).

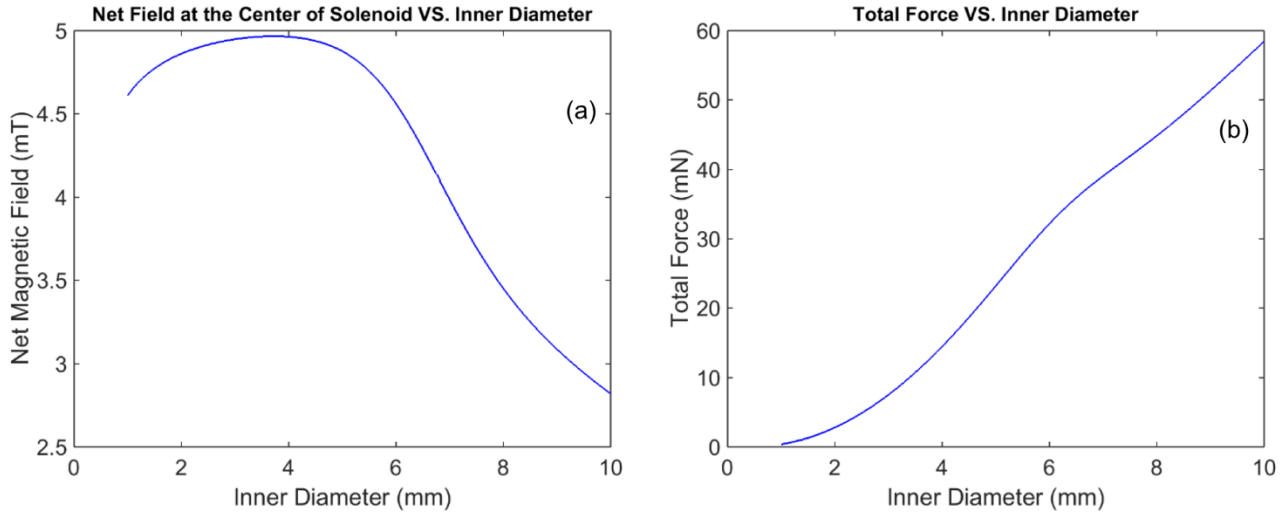

Figure 7. a) Net magnetic field at the center of each coil of the actuator versus coil inner diameter. (l_w, wire length=3m, permanent magnet length=10mm, b) The total force of the actuator versus coil inner diameter. (l_w(wire length)=3m, permanent magnet length=10mm)

Figure 7(a) shows a maximum magnetic field at *4mm*. When the inner diameter enlarges more than almost *4mm*, the magnetic field decreases due to the increase in distance vector ($\vec{r}$) length. On the other hand, since the total force is proportional to the square of the

inner diameter, it eventually grows as inner diameter rises (Figure 7(b)). Since the wire length and applied current are constant, all different coil combinations consume equal electrical powers.

3. *Solenoid Geometry Design Optimization*

In this section, determination of optimal values for coil geometry is discussed in order to obtain maximum magnetic field strength at the center of coil bounding the consumed electrical power. We restrict the solenoid's wire length (l_w) affecting the resistance also flowing current ($0.33amp$) through the conductor to ensure a certain amount of power consumption. The geometrical properties of a coil include the solenoid length, l, the inner and outer diameter (d_i, d_o respectively) and the number of coil turns, N. According to the previous section analytical results (Figure 7(b)) the solenoid force has an ascending relationship with solenoid inner diameter. However, the magnetic field reaches the maximum nearly *4mm* inner diameter, which is determined for the optimization analysis. In order to find optimal solenoid length, we studied the distribution of certain wire length (l_w=3m) over different coil lengths varies from *0.16mm* (the wire diameter) in a flat spiral coil to *42mm* in a one-layer long coil. We performed this wide range of coil turn distribution from the multi-layer planar coil all the way to the one-layer one just to get the idea that how the optimal geometry would be look like. Applying z=0 in equation 5, which means selecting the arbitrary point (P) at the central loop, gives the maximum magnitude of the magnetic field at the center of the solenoid (Figure 8(a)). Also, Force resulted from the interaction of the coil and the magnetic core is presented in Figure 8(b).

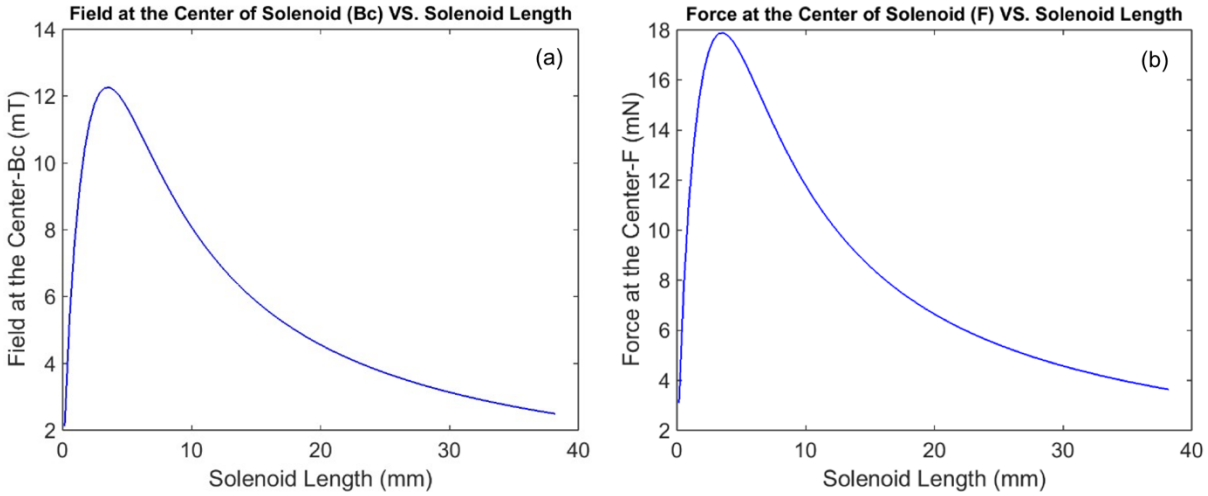

Figure 8. a) The magnetic field at the center of solenoid versus the solenoid length for a fixed-length wire $(l_w = 3m)$*, b) Force at the center of solenoid versus the solenoid length for a fixed-length wire* $(l_w = 3m)$

The final goal of this section is to obtain an optimal multilayer geometry for the coil, therefore we need to know how various geometrical parameters of a coil are correlated to each other. It is worth noting that, the radius in equation 5 must be the coil average radius($d_a/2$) which is the function of turn numbers (N) and circle packing density (λ). Circle packing density is the ratio of the cross-section taken up by the wires to the available space. The maximum packing density is for the hexagonal lattice circle packing arrangement shown in Figure 9 which has a packing density of $\pi/\sqrt{12}$ (Schimpf 2013; Weisstein n.d.).

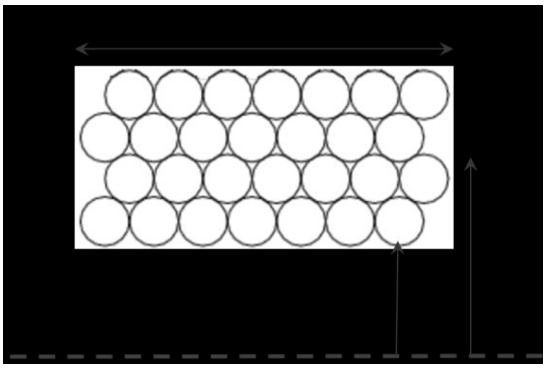

Figure 9. Coil axial cross section and packing density (λ); $d_i/2$*: coil inner radius,* $d_a/2$*: coil average radius, l: coil length.*

The relationship among coil average and internal diameters (d_a,d_i), coil length (l), packing density (λ), turn numbers (N) and wire cross section(a) explained in detail in (Schimpf 2013) as follows in equation 16:

$$\lambda(d_a - d_i)l = Na$$
$$d_a = \frac{a}{\lambda l} N + d_i \quad (15)$$

Moreover, N is also considered a function of average diameter (d_a) and wire length (l_w) by itself as expressed in equation 17.

Therefore, the turn density ($n = \frac{N}{l}$) is a function of wire length and average diameter.

$$N = l_w / \pi d_a \quad (16)$$

Figure 10 depicts the variation of the solenoid's average and external diameter with respect to solenoid length. Average diameter falls significantly as solenoid length grows.

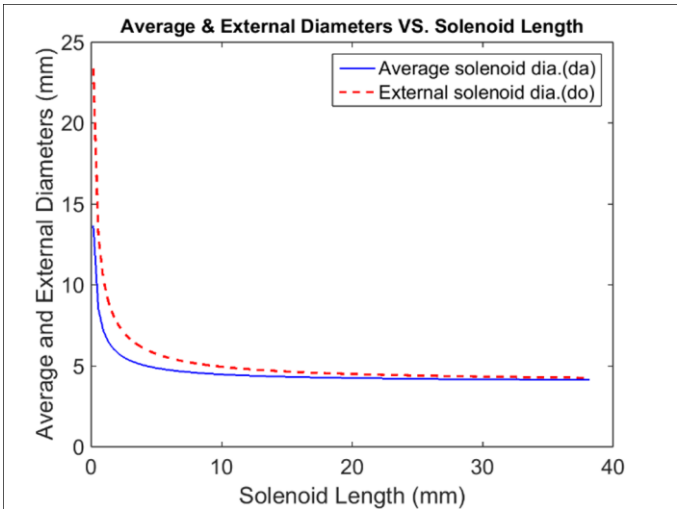

Figure 10. Average and external diameters versus solenoid Length

Figure 11 illustrates the changes in solenoid turns (N) versus solenoid length. The increase in N is due to the drastic decrease in average solenoid diameter while solenoid length rises.

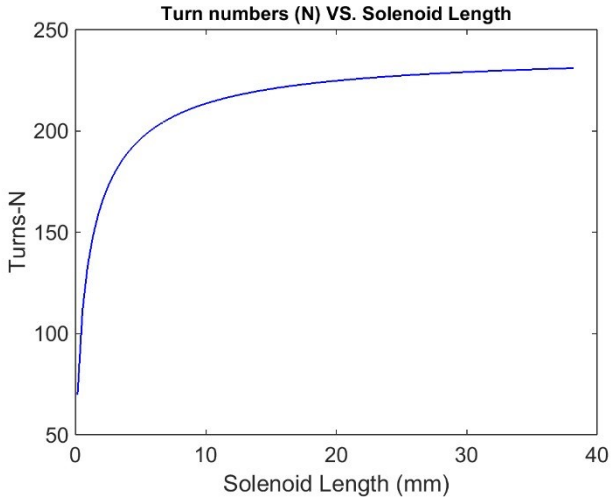

Figure 11. Solenoid turns versus solenoid length for a fixed-length wire ($l_w = 3m$)

In all coil configurations investigated above, the wire length and flowing current kept identical so, the electrical power consumption for all of them is $P = RI^2 = 0.2797$ Watts.

The goal is to gain the maximum force out of a certain cross-sectional area of the solenoid. Hence, we maximized the ratio of force to cross-section (F / A) where A is the cross-section of the solenoid calculated by the external coil diameter (d_o). Figure 14 illustrates how the (F / A) ratio varies with respect to the solenoid length.

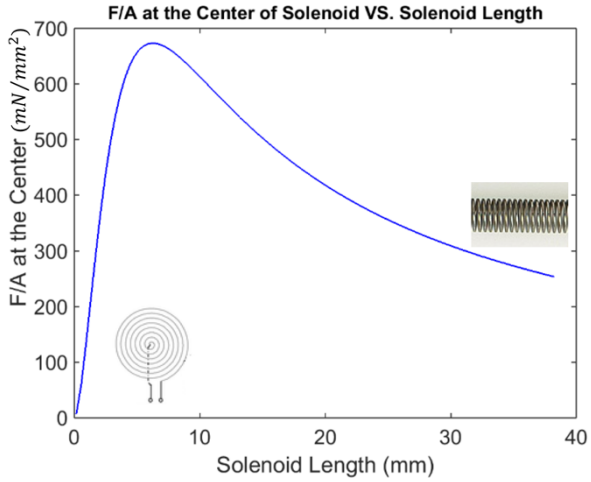

Figure 12. Force to solenoid cross-section ratio at the center of solenoid versus solenoid length for a fixed-length wire ($l_w = 3m$)

The optimal amount for the solenoid length according to the graph in Figure 12 is l =6.4mm which maximize the force to cross-section ratio to the amount of $662 mN/mm^2$. The corresponding turn numbers, average coil diameter and external coil diameter at this optimum length obtained from graphs in Figure 10 and Figure 11 as d_a =4.7mm, d_o =5.4mm and N≈215 turns respectively.

The aforementioned solenoid optimal geometry also maximizes the (F / A) ratio drawn versus the solenoid cross-section in Figure 15.

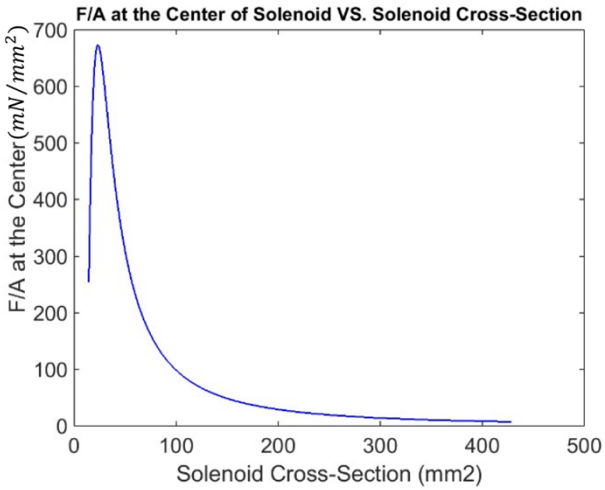

Figure 13. Force to solenoid cross-section ratio at the center of solenoid versus solenoid cross-section for a fixed-length wire ($l_w = 3m$)

Conducting the analytical optimization above we found an optimum solenoid geometry for embedding in the electromagnetic actuator structure to maximize the exerting force out of the solenoid size while bounding the power consumption to a certain amount. The optimal coil geometry composed of almost 215 turns in 40 columns and nearly 5 layers. The coil inner and outer diameters are d_i =4mm and d_o =5.4mm. According to the graphs presented in Figure 8(a) and 8(b), the maximum amounts for the magnetic field and force at the center of the designed optimal coil are B_{max} =12.26mT and F_{max} =17.88mN respectively.

Figure 12 and Figure 13 illustrate that increasing the size of the solenoid actuator leads to a drastic decrease in the actuation force. The diagrams have an ascending trend on the small beginning portion of the diagram where the solenoid sizes are smaller than the optimum one. From the peak point onwards, the actuation force decreases by enlarging the solenoid. In other words, the proposed solenoid actuator is scalable and has generally the capability of generating higher forces by getting smaller. Figure 14, in addition, strongly confirms this finding as it has almost the same behavior since the solenoid force drops significantly by increasing the volume of the solenoid. This characteristic enables one to exert higher forces by combining several tiny actuators rather than using just a larger one. However, there are some limitations in scaling down the size of the actuator which are discussed in the following section.

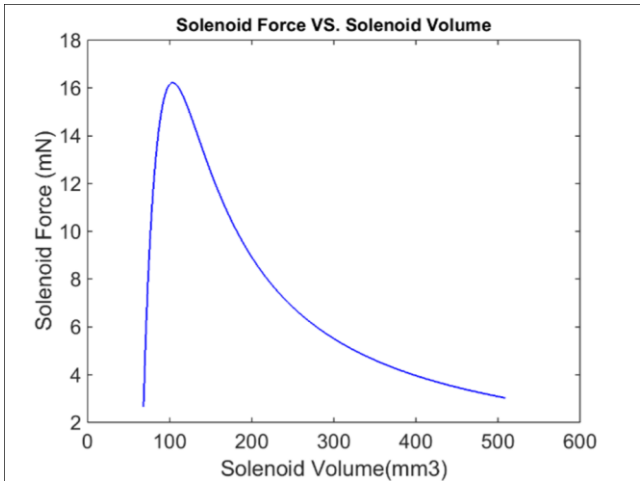

Figure 14. Force at the center of solenoid versus the solenoid volume for a fixed-length wire ($l_w = 3m$)

In Figure 15 we compared various coil inner diameters in terms of three parameters: magnetic field, force, and force to cross-section ratio. It verifies that our selection for inner diameter, *4mm*, generates the maximum F / A among the other options.

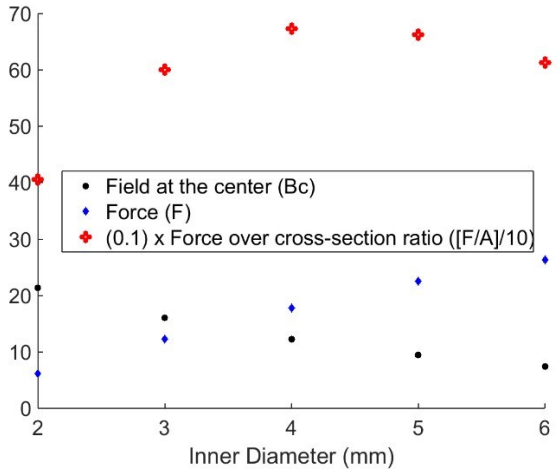

Figure 15. Comparison of the magnetic field, force, and force to cross-section ratio for different coil inner diameters (2,3,4,5 and 6 mm)

4. Manufacturing Aspects and Limitations

In this section, the restrictions of scaling down the size of the actuator are discussed. In the previous section, we just selected a constant wire length and diameter to bound the power consumption and optimize the geometry of the coil to generate higher forces. Regarding such constraints, we found some relatively small dimensions for the solenoid which optimize the generated force. It was argued that enlarging those dimensions causes less force to cross-section or force to volume ratios. Although, the applied constraints over the wire length and its diameter are originated in some manufacturing and implementation restrictions. We studied various wire lengths as well as wire diameters to show how they affect the generated force and power consumption.

Firstly, we considered coils with different wire length having the same diameter (34AWG) as presented in Table 1. The results show that longer wires consume more power, generate larger coils which produce more force to size ratio. However, the last column of the table compares the generated force over the size and consumed power. Comparing the last column of Table 1, as expected, the smaller coil made up of the shorter wire is the most effective option. Despite the efficiency of the mentioned coil, it is not executable thanks to its small size ($d_i = 1.85mm$). Therefore, the wire length of 3m was chosen for the optimization study.

Table 1.Comparison of coils with various wire lengths but the same wire diameter (34AWG)

Wire Length (lw)-m	***Optimum inner dia. (di)-mm***	***Optimum coil length (l)-mm***	***Consumed power (P)-Watt***	***Force to cross-section ratio (F/A)***	***Force to cross-section to power ratio (F/AP)***
1	1.85	5.29	0.0932	325	3.48×10^3
2	2.98	5.85	0.1864	541	2.90×10^3
3	3.69	6.44	0.2797	662	2.37×10^3
4	4.39	6.91	0.3729	756	2.03×10^3
5	4.82	7.39	0.4661	827	1.78×10^3

Secondly, we studied coils composed of equal wire length (l_w =3m) but different diameters. Since the wire diameters are different, the allowable applying current ("American Wire Gauge Chart and AWG Electrical Current Load Limits Table with Skin Depth Frequencies and Wire Breaking Strength" n.d.) varies in each case as well as the resistance per length ("American Wire Gauge" 2018), both presented in Table 2. In this case again the finest wire (40AWG) generates the highest amount of force to cross-section to power ratio among the other cases (Table 2). Even though, due to the very fine geometry of the correlated coil (d_i =2.27mm) and small allowable current (I =0.09A) it is not applicable. Consequently, the wire size 34AWG was selected.

Table 2. Comparison of coils with various wire dia. but the same wire length (lw=3m)

Wire Gauge	***Wire dia. (dw)-mm***	***Resistance/length-(mΩ/m)***	***Allowable current-A***	***Optimum inner dia. (di)-mm***	***Optimum coil length (l)-mm***	***Force to cross-section to power ratio (F/AP)***	***Force to cross-section ratio (F/A)***
34AWG	0.160	856	0.33	3.7	6.4	2.36	0.66
36AWG	0.127	1361	0.21	3.1	5.6	3.04	0.55
38AWG	0.101	2164	0.13	2.7	4.8	3.99	0.44
40AWG	0.0799	3441	0.09	2.3	4.1	4.65	0.39

Hence, there are some factors contribute in practical manufacturing and experimental condition confining our selection of the optimum coil for the electromagnetic actuator.

5. The Influence of Solenoid Section Deformation on the Magnetic Field and Force

The actuator might undergo some squeezing and loses its round shape under the transverse loads. In this section, we are going to study the compressive effect on the resultant magnetic field. Under radial load, circular cross-section turns into the ellipse and then by increasing the load eccentricity of the elliptical cross-section will increase. In the following we consider the resulting magnetic field of a planar elliptical current carrying conductor at the center of the geometry and then investigate the effect of ellipse eccentricity on the field. For this purpose, we consider a current carrying elliptical wire geometry and then again use Biot-Savart law to explicitly calculate the magnetic field due to the flowing current. This law gives the total magnetic field at an arbitrary point P in the space by superposition of magnetic field contributors. Having vectorial form, only a few simple conductor geometries lead to an analytical evaluation of the magnetic field and shapes other than a circular or straight wire leads to some complicated integral calculations (Miranda 2000). Applying polar coordinates for general equation of conic sections (including ellipse) and using a vectorial form of Biot-Savart law, an equation for the magnetic field has been derived in (Christodoulides 2009; Schroeder 2017). However, it is valid just at a focus of the sections.

Using polar coordinate system for the expression of wire's geometry, Miranda in (Miranda 2000) proposed a very simple line integral (equation 18) using Biot-Savart law in scalar form in order to calculate the magnitude of magnetic field due to arbitrary shapes of planar current-carrying conductors at a point belongs to the plane of wire.

$$\mathrm{B} = \frac{\mu_0 I}{4\pi} \oint \frac{d\theta}{r} \tag{17}$$

Where $r = r(\theta)$is the expression of wire geometry in polar coordinate and measured from the observation point (O) located in the same plane with the wire (Smythe 1989; Miranda 2000; Spiegel and Liu 1999). For an elliptical wire geometry shown in Figure 16, the element of ds normal to r is $rd(\theta)$. In addition, $x=r\cos\theta$ and $y=r\sin\theta$ so that the line integral above expresses as the following:

$$B = \frac{\mu_0 I}{4\pi} \oint \frac{\sqrt{a^2 \sin^2\theta + b^2 \cos^2\theta}\, d\theta}{ab} \quad (18)$$

Since, for ellipse geometry $\frac{x^2}{a^2} + \frac{y^2}{b^2} = 1, 1 = \frac{r^2 \cos^2\theta}{a^2} + \frac{r^2 \sin^2\theta}{b^2} = r^2 a^{-2} b^{-2} (b^2 \cos^2\theta + a^2 \sin^2\theta)$.

On the other hand, the area of the ellipse is

$$A = \pi ab \quad (19)$$

And the perimeter is

$$\oint \sqrt{dx^2 + dy^2} = \oint \sqrt{a^2 \sin^2\varphi + b^2 \cos^2\varphi}\, d\varphi = P \quad (20)$$

Since, the parametric form of the ellipse equation is $x = a\cos\varphi$, $y = b\sin\varphi$; $dx = -a\sin\varphi d\varphi$ and $dy = a\cos\varphi d\varphi$. Substituting equations 14 and 20 in 13, results:

$$B = \frac{1}{4}\mu_0 I\, P/A \quad (21)$$

So, the magnitude of the magnetic field at the center of an elliptical conductor is proportional to the ratio of the circumference to the area.

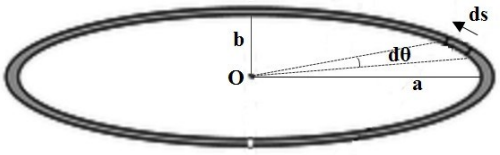

Figure 16. Current element on the elliptical conductor loop; a: semi-major axis of the ellipse, b: semi-minor axis of the ellipse, differential length element on the elliptical current carrying loop.

We were interested to find the impact of solenoid section deformation on the magnetic field at the center. Considering equation 14, for a one loop circular section with specific perimeter we studied the effect of section deformation as a function of ellipse eccentricity $(0 \le e = c/a < 1)$ as the circular section undergoes deformation and turns to an ellipse. The parameter "c" is the distance from the center to a focus of the ellipse. Figure 17 depicts the variation of magnetic field versus elliptical eccentricity beginning from $e = 0$ for a round circular coil section and growing to $e < 1$ for a squeezed oval coil.

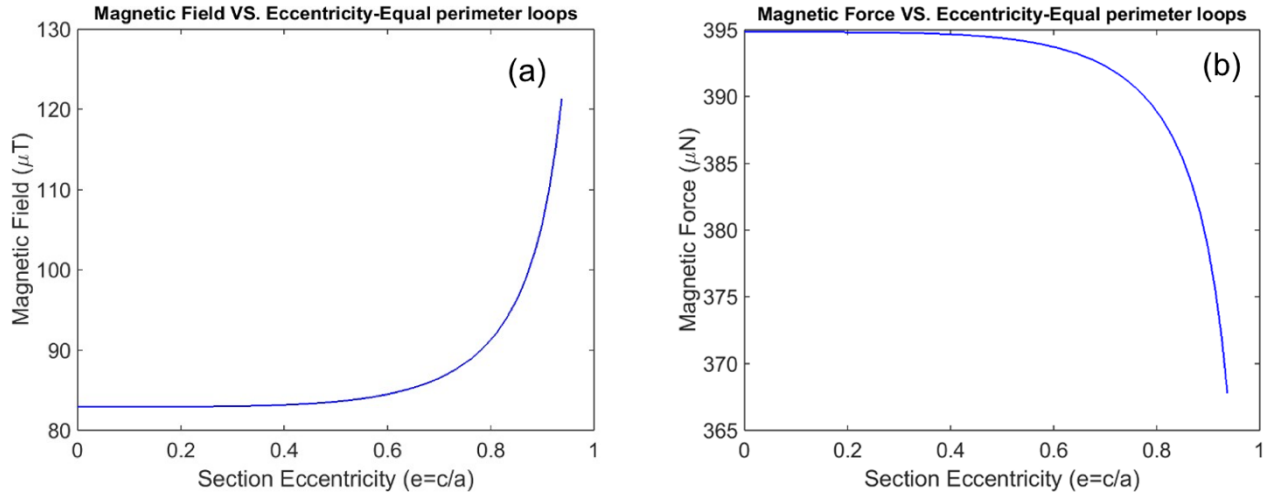

Figure 17. a) Magnetic field changes due to deformation of one current carrying loop section, b) Magnetic force changes due to deformation of one current carrying loop section

Figure 17(a) depicts a drastic growth in the magnetic field at the center of a current carrying loop at *e=0.8* showing that the compressed and oval cross section of a solenoid escalates the resultant magnetic field at the center. However, because of the decrease in cross-section of the squeezed and oval cross-section the magnetic core cross section also decreased leads to a significant drop in magnetic force shown in Figure 17(b).

Maintaining a constant cross-section, we are interested to compare the magnetic field and force of circular and elliptical shapes respectively. Figure 18(a) and 18(b) compare axial magnetic fields and forces for elliptical current carrying loops having the same cross-section areas but different perimeters and eccentricity. As depicted in the graphs, both of the parameters show significant rises around *e=0.8*. In this case, because of the constant cross-sections, the force has also an ascending trend similar to the magnetic field.

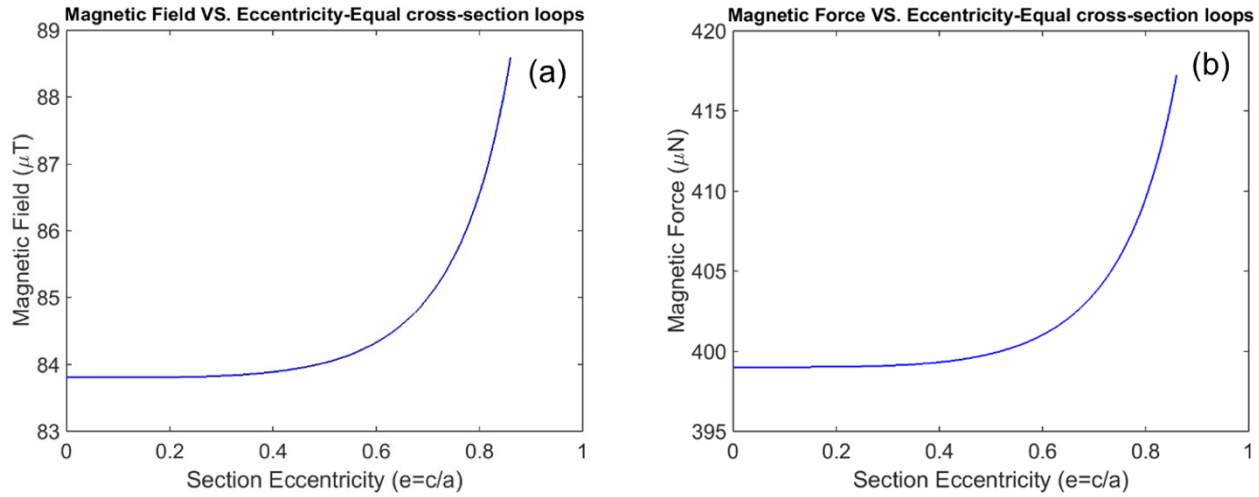

Figure 18. a) Magnetic fields of elliptical current carrying loops with equal cross-sections but different perimeters and eccentricities, b) Magnetic forces of elliptical current carrying loops with equal cross-sections but different perimeters and eccentricities

6. *Discussion and Conclusion*

This article discusses design optimization of a cylindrical solenoid with a permanent magnet core as the main component of the electromagnetic actuator. The magnetic field and resultant force of the solenoid are formulized using Biot-Savart law and the charge model respectively. Equations 5 and 14 denote the geometrical and physical parameters contributing in the magnetic field and force respectively. The impact of cylindrical coil inner diameter (d_i) on the magnetic field and force examined for a constant wire length.

Figure 7(a) and 7(b) show the dependency of the magnetic field and force to the inner diameter for a constant current passing throughout the coil. Since the assumption of fixed wire length is considered the average diameter decreases as the coil length increases. Therefore, the number of turns increases, up to a point where a single layer is reached. Results show that an increase in turn numbers leads to an increase in both the magnetic field and force. We obtained an optimal value for the coil inner diameter which maximized the magnetic field and later used this value to optimize the geometry so that it maximizes the force to the solenoid cross-section ratio. As the inner diameter increases, the force enhances due to the increased magnetic core cross section.

According to the mentioned calculation for magnetic field and force, a solenoid geometrical design optimization was discussed. For this study, a coil with a constant inner diameter and varying length was investigated. The magnetic field at the middle of the coil maximized while the electrical power consumption was restricted by means of using a particular amount of wire length with a specific wire cross section and also applying a constant current in the calculations. The applied current was chosen regarding the wire gauge current restrictions. Using packing density factor and applying average diameter (d_a) in the relevant equations, the magnetic field at the middle of the coil shows a maximum around a certain coil length. Hence, we got an optimized geometry of the coil in order to get the maximum magnetic field in the middle while its power consumption is restricted.

We then investigated the effect of scaling down the coil size and surprisingly found that the smaller the coil's size the more force to cross-section ratio for the constant consumed power situation as well as more force to cross-section to power ratio in case that power consumption is not restricted as illustrated in Figure 13, Figure 14, Table 1, and Table 2.

Next, since the coil might undergo some deformity due to the lateral forces, we investigated the effect of solenoid cross-section compression turning the section from circle to oval shapes with different degrees of ellipticity. For this purpose, we used a simplified form of Biot-Savart law toward the calculation of magnetic field at the center of the elliptic geometry and then formulized it for various ellipses with the same circumference yet various cross-sections. Keeping constant perimeter (P) for the coil section, the growth in elliptical eccentricity causes a decrease in the cross-section area (A) and thus raises the resultant magnetic field at the center

since it is proportional to the ratio of ellipse perimeter to its cross section. The coil cross-section deformation into oval increases the magnetic field at the center as illustrated in Figure 17. The graph shows the dependency of the magnetic field at the center of a constant perimeter geometry varies from a circle to squeezed ellipses. It initiates a significant escalation around the eccentricity of *e=0.8*. However, section squeezing decrease the cross section causes a sharp drop in the resultant force. Studying elliptical sections with the same cross-section areas but different perimeters and eccentricities show significant increases in both magnetic field and forces at the center of the current carrying loop as section eccentricity increases.

Acknowledgment

This work is supported by the National Science Foundation under Grant No.1850898.

References

"American Wire Gauge." 2018. *Wikipedia*. https://en.wikipedia.org/w/index.php?title=American_wire_gauge&oldid=849031042.

"American Wire Gauge Chart and AWG Electrical Current Load Limits Table with Skin Depth Frequencies and Wire Breaking Strength." n.d. Accessed July 26, 2018. http://www.powerstream.com/Wire_Size.htm.

Banick, Gerard S., and John J. Haller. 1991. Solenoid actuator having a magnetic flux sensor. United States US5032812A, filed March 1 , 1990, and issued July 16, 1991. https://patents.google.com/patent/US5032812A/en.

Christodoulides, Costas. 2009. "The Magnetic Field Produced at a Focus of a Current-Carrying Conductor in the Shape of a Conic Section." *American Journal of Physics - AMER J PHYS* 77 (December): 1195–96. https://doi.org/10.1119/1.3183888. Ebrahimi, Nafiseh, Noughro S, Gao, Wei, Taha Ahmad, Jafari Amir. 2018 " Dynamic Actuator Selection and Robust State-Feedback Control of Networked Soft Actuators" Proceeding of IEEE International Conference on Robotic and Automation (ICRA 2018).

Fries, F., S. Miyashita, D. Rus, R. Pfeifer, and D. D. Damian. 2014. "Electromagnetically Driven Elastic Actuator." In *2014 IEEE International Conference on Robotics and Biomimetics (ROBIO 2014)*, 309–14. https://doi.org/10.1109/ROBIO.2014.7090348.

Furlani, Edward P. 2001. Permanent Magnet and Electromechanical Devices: Materials, Analysis, and Applications. Academic Press.

Grandy, Walter T. Jr. 2012. Introduction to Electrodynamics and Radiation. Elsevier.

Guo, Rui, Lei Sheng, HengYi Gong, and Jing Liu. 2018. "Liquid Metal Spiral Coil Enabled Soft Electromagnetic Actuator." *Science China Technological Sciences* 61 (4): 516–21. https://doi.org/10.1007/s11431-017-9063-2.

Jiles, David C. 1998. Introduction to Magnetism and Magnetic Materials, Second Edition. CRC Press.

Kamal, Manish, and Glenn S. Daehn. 2007. "A Uniform Pressure Electromagnetic Actuator for Forming Flat Sheets." *Journal of Manufacturing Science and Engineering* 129 (2): 369–79. https://doi.org/10.1115/1.2515481.

Lim, K. W., N. C. Cheung, and M. F. Rahman. 1994. "Proportional Control of a Solenoid Actuator." In*, 20th International Conference on Industrial Electronics, Control, and Instrumentation, 1994. IECON '94*, 3:2045–50 vol.3. https://doi.org/10.1109/IECON.1994.398134.

Miranda, José A., "Magnetic Field Calculation for Arbitrarily Shaped Planar Wires." *American Journal of Physics* 68 (3): 254– 58 . https://doi.org/ 10.1119/1.19418.

Mitsutake, Y., K. Hirata, and Y. Ishihara. 1997. "Dynamic Response Analysis of a Linear Solenoid Actuator." *IEEE Transactions on Magnetics* 33 (2): 1634–37. https://doi.org/10.1109/20.582582.

Panofsky, Wolfgang K. H., and Melba Phillips. 2012. *Classical Electricity and Magnetism: Second Edition*. Courier Corporation.

Petit, L., C. Prelle, E. DorÉ, F. Lamarque, and M. Bigerelle. 2010. "A Four-Discrete-Position Electromagnetic Actuator: Modeling and Experimentation." *IEEE/ASME Transactions on Mechatronics* 15 (1): 88–96. https://doi.org/10.1109/TMECH.2009.2017018.

Pratt, Teryl L. 2008. Charge Model Expansion of the Standard Model of Particle Physics. BookSurge Publishing.

Rawlik, M., C. Crawford, A. Eggenberger, K. Kirch, J. Krempel, F. M. Piegsa, and G. Quéméner. 2017. "A Simple Method of Coil Design." *ArXiv:1709.04681 [Physics]*, September. http://arxiv.org/abs/1709.04681.

Said, Muzalifah Mohd., Jumril Yunas, Roer Eka Pawinanto, Burhanuddin Yeop Majlis, and Badariah Bais. 2016. "PDMS Based Electromagnetic Actuator Membrane with Embedded Magnetic Particles in Polymer Composite." *Sensors and Actuators A: Physical* 245 (July): 85–96. https://doi.org/10.1016/j.sna.2016.05.007.

Schimpf, Paul. 2013. "A Detailed Explanation of Solenoid Force." *International Journal on Recent Trends in Engineering & Technology (IJRTET)* 8 (January): 7–14.

Schroeder, Daniel V. 2017. “Entanglement Isn’t Just for Spin.” *American Journal of Physics* 85 (11): 812–20. https://doi.org/10.1119/1.5003808.

Shin, Bu Hyun, Seung-Wook Choi, Young-Bong Bang, and Seung-Yop Lee. 2011. “An Earthworm-like Actuator Using Segmented Solenoids.” *Smart Materials and Structures* 20 (10): 105020. https://doi.org/10.1088/0964-1726/20/10/105020.

Smythe, William R. 1989. *Static And Dynamic Electricity*. 1 edition. New York, NY: CRC Press.

Song, Chang-Woo, and Seung-Yop Lee. 2015. “Design of a Solenoid Actuator with a Magnetic Plunger for Miniaturized Segment Robots.” *Applied Sciences* 5 (3): 595–607. https://doi.org/10.3390/app5030595.

Spiegel Murray R., and Liu John. 1999. *Mathematical Handbook of Formulas and Tables*. McGraw-Hill.

Weisstein, Eric W. n.d. “Circle Packing.” Text. Accessed May 8, 2018. http://mathworld.wolfram.com/CirclePacking.html.